Monthly Notices
of the
ROYAL ASTRONOMICAL SOCIETY

MNRAS **475,** 1819–1828 (2018)
Advance Access publication 2017 December 22

doi:10.1093/mnras/stx3302

Cosmic ray processing of N_2-containing interstellar ice analogues at dark cloud conditions

G. Fedoseev,* C. Scirè, G. A. Baratta and M. E. Palumbo

INAF – Osservatorio Astrofisico di Catania, via Santa Sofia 78, I-95123 Catania, Italy

Accepted 2017 December 13. Received 2017 December 13; in original form 2017 April 4

ABSTRACT

N_2 is believed to lock considerable part of nitrogen elemental budget and, therefore, to be one of the most abundant ice constituent in cold dark clouds. This laboratory-based research utilizes high energetic processing of N_2 containing interstellar ice analogues using 200 keV H^+ and He^+ ions that mimics cosmic ray processing of the interstellar icy grains. It aims to investigate the formation of (iso)cyanates and cyanides in the ice mantles at the conditions typical for cold dark clouds and prestellar cores. Investigation of cosmic ray processing as a chemical trigger mechanism is explained by the high stability of N_2 molecules that are chemically inert in most of the atom- and radical-addition reactions and cannot be efficiently dissociated by cosmic ray induced UV-field. Two sets of experiments are performed to closer address solid-state chemistry occurring in two distinct layers of the ice formed at different stages of dark cloud evolution, i.e. 'H_2O-rich' and 'CO-rich' ice layers. Formation of HNCO and OCN^- is discussed in all of the performed experiments. Corresponding kinetic curves for HNCO and OCN^- are obtained. Furthermore, a feature around 2092 cm^{-1} assigned to the contributions of ^{13}CO, CN^-, and HCN is analysed. The kinetic curves for the combined HCN/CN^- abundance are derived. In turn, normalized formation yields are evaluated by interpolation of the obtained results to the low irradiation doses relevant to dark cloud stage. The obtained values can be used to interpret future observations towards cold dark clouds using James Webb Space Telescope.

Key words: astrochemistry – solid state: volatile – methods: laboratory: solid state – techniques: spectroscopic – ISM: molecules – infrared: ISM.

1 INTRODUCTION

The chemistry of nitrogen-bearing species in star-forming regions of the interstellar medium (ISM) presents a particular interest for astrochemists because of its potential to reveal the formation routes of the simplest amino acids, nucleobases, or their potential precursors. The latter formation routes usually involve various 'CN-bearing' species, such as HCN (hydrogen cyanide), HNCO (hydrogen isocyanate), H_2NCHO (formamide), H_2NCH_2CN (aminoacetonitrile), etc. (Minard et al. 1975; Belloche et al. 2008; Matthews & Minard 2008; Danger et al. 2011; Fedoseev et al. 2015; Saladino et al. 2016). These suggested formation routes can be best illustrated on the example of HCN, see fig. 1 of Matthews & Minard (2008). Polymerization of HCN upon thermal and energetic processing results in the formation of oligomers with various structures including branched and polycyclic structures. Their subsequent hydrolysis results in the formation of oligopeptides (that can be further hydrolysed to the individual amino acids) along with the simple aromatic nitrogenous bases, including nucleobases. Similar formation mechanism can be proposed for the formation of oligopeptides by irradiation of interstellar ice analogues containing HNCO, see fig. 6 of Fedoseev et al. (2015), where HNCO molecules play a role of the future peptide bonds in the formed oligomers. On the other hand, it has been shown that condensation of H_2NCHO molecules results in the formation of few nucleobases (Saladino et al. 2006). Thus, the derivation of formation yields for the 'CN-bearing' species already detected in the ISM, such as (iso)cyanates and cyanides, and the prediction of formation routes of previously undetected species are important goals for laboratory-based astrochemistry.

Systematic mid-infrared (IR) observations of cold molecular clouds and Young Stellar Objects (YSOs) with ISO and *Spitzer* infrared space telescopes, allowed the exploration of wavelength ranges previously inaccessible from Earth. A comparison of this newly acquired IR data with the laboratory IR spectra of various mixed ices recorded at cryogenic temperature conditions greatly improved our knowledge on the composition of icy grain mantles in these regions (Gibb et al. 2004; Öberg et al. 2011; Boogert, Gerakines & Whittet 2015). Two distinct ice formation stages take place during dark molecular cloud evolution and set up the initial ice

* E-mail: gfedo@oact.inaf.it

composition for further star formation stages. At first, less-volatile 'H_2O-rich ice' is formed on the grain surface from accreting atoms (e.g. H, O, N, etc.) and simplest molecules. This ice layer is enriched with solid NH_3, CH_4, and CO_2. During this stage, most of the accreting CO molecules interact with OH radicals yielding CO_2 (Chang & Herbst 2012; Ioppolo et al. 2013). With the increase of density and corresponding decrease of temperature and photodesorption rates, a 'rapid' freeze-out of CO molecules occurs and 'CO-rich ice' layer is formed on top of the previously produced 'H_2O-rich ice'. The accreted CO-molecules, in turn, interact with accreting H-atom and produce most of the solid CH_3OH observed in cold prestellar cores. The 'CO-rich' ice layer is also associated with the observation of so-called 'XCN' absorption feature at 4.62 μm often assigned to OCN^- (cyanate ion). 'XCN' absorption feature is only observed in high- and low-YSOs and its formation may require energetic or thermal processing by the newly formed protostar (Tielens et al. 1991; Gibb et al. 2004; Öberg et al. 2011; Mathews et al. 2013; Boogert, Gerakines & Whittet 2015).

From over 180 species unambiguously identified in the ISM, about one-third contains nitrogen atoms, however, only three nitrogen-bearing species are usually discussed in the context of solid-state observations. These are NH_3 with the relative abundance of 4–8 per cent with respect to H_2O ice; aforementioned OCN^- that is usually assigned to the whole or a part of so-called 'XCN' absorption feature at 4.62 μm and has abundance of 0.3–0.8 per cent; and NH_4^+ that can be one of the carriers of the 6.85 μm band with abundance as high as 15 per cent (Öberg et al. 2011; Boogert, Gerakines & Whittet 2015). Formation of NH_4^+ gets further support because both NH_4^+ and OCN^- can be efficiently formed in the single reaction from two precursor molecules, NH_3 and HNCO (Demyk et al. 1998; van Broekhuizen, Keane & Schutte 2004; van Broekhuizen et al. 2005). Nevertheless, these three species only accounts for 15–30 per cent of the total nitrogen elemental budget. So far, most of the elemental nitrogen is believed to be locked in solid N_2 that is insensitive to mid-IR observations due to the lack of dipole moment in this homonuclear molecule. Thus, only indirect proves of its presence can be found, see Elsila, Allamandola & Sandford (1997), Sandford et al. (2001), and Boogert, Blake & Tielens (2002, 2015). The latter works provide the upper limit on the amount of solid N_2 with respect to H_2O ice ranging from 0.2 to 60 per cent.

Although N_2 may appear to be the most abundant nitrogen-bearing species in the cold dark clouds and prestellar cores, so far it draws little attention in the solid-state astrochemistry. Triple N≡N bond is the strongest molecular bond, therefore, N_2 demonstrates near complete inertness towards atom-addition reactions and is 'near-transparent' to Ly-α radiation requiring photons with >12 eV energy to be efficiently dissociated and participate in UV-induced solid-state reactions (Wu et al. 2012; Li et al. 2013; Islam, Baratta & Palumbo 2014). This explains the choice of high-energetic ion irradiation (mimicking cosmic rays processing) as the main chemical trigger of N_2 chemistry in cold molecular clouds.

This research aims at better understanding of cosmic ray induced N_2 chemistry in cold molecular clouds, and perceives two following goals:

(i) to present the overall formation yields of few chosen 'CN-bearing' species for the irradiation doses relevant to the earliest star formation stage—cold dark cloud;

(ii) to investigate the possibility of utilizing these formation yields as an indirect probe of N_2-presence in the icy grain mantles in cold dark clouds.

To achieve these goals, a detailed quantitative analysis of irradiation products obtained after ion processing of few chosen N_2-containg ice mixtures with 200 keV H^+ and He^+ ions is performed. The choice of the initial compositions in irradiated ice mixtures is aimed to somehow address the cosmic ray processing of solid N_2 in both 'H_2O-rich' and 'CO-rich' ice layers of the interstellar icy grain mantles. H_2O:CH_4:N_2 (1:1:1) and H_2O:CH_4:NH_3 (1:1:1) mixtures are chosen to address N_2 chemistry in 'H_2O-rich polar ice' and the relative difference between irradiation of NH_3 and N_2 containing ices. While CH_3OH:N_2 (1:1) and CO:CH_4:N_2 (1:1:1) mixtures are chosen to address N_2 chemistry in 'CO-rich' ice layers. The main difference from the previous studies devoted to the cosmic ray processing of N_2-containing interstellar ice analogues lies in the acquisition of the kinetic curves for the chosen products. The obtained kinetic curves are used for investigation of irradiation doses as low as 0.05 eV/16 u. This is achieved by interpolation of the obtained results in the range from 0 to 10 eV/16 u.

HNCO and OCN^- kinetic curves are obtained in each of the performed experiments and the corresponding formation yields are derived. The analysis is completed by presentation of the similar kinetic curves and the formation yields for the combined HCN and CN^- abundances. Acquisition of these values is particularly important in view of the future James Webb Space Telescope (JWST) observations that can provide more insights on the composition of 'XCN' absorption feature in YSOs, or present the first observation of HNCO or OCN^- in dark clouds using background star observations.

2 EXPERIMENTAL DETAILS AND DATA REDUCTION

2.1 Experimental setup

All experiments are performed using the experimental setup previously described by Strazzulla et al. (2001) and Baratta et al. (2015). It consists of two distinct stainless steel vacuum chambers, a main Ultra High Vacuum (UHV) chamber and a High Vacuum (HV) ion-beamline. A sample holder is mounted on the cold head of a He close-cycle cryostat placed in the centre of the main UHV chamber. The temperature control is realized by means of a resistor and a diode temperature sensor, enabling the range of substrate temperature from 300 down to 12 K. The relative temperature uncertainty among different experiments is lower than 1 K.

The base pressure in the main chamber is $\sim 1.5 \times 10^{-9}$ mbar achieved through the application of an ion pump. The ion-beam line connects the main chamber with the ion implanter and is pumped down to 2×10^{-7} mbar to allow a collision-free path of the ion beam. A gate valve is placed between the two chambers to allow their independent operation. Two KBr view ports are installed on the main chamber orthogonal to the path of the ion beam to allow for the acquisition of transmittance IR spectra using a Bruker Equinox 55 or Bruker Vertex 70 FTIR spectrometers. In particular, the substrate plane is fixed at an angle of 45 deg with respect to both the IR beam and the ion beam. In this way it is possible to collect transmittance IR spectra *in situ*, even during the ion bombardment, without tilting the sample. A rotatable polarizer placed along the path of the IR beam allows to take spectra at oblique incidence both with the electric vector parallel (p-polarized) and perpendicular (s-polarized) to the plane of incidence. The ices are grown utilizing background deposition technique on KBr or silicon substrates by introducing the gas mixtures into the vacuum chamber through an all-metal needle valve. The applied background deposition results in the formation

of an uniform ice surface on the front side of the substrate, while the ice deposition on the backside of the substrate is prevented by the installation of a copper cold shield with a 20 mm long narrow tube aligned along the path of the IR beam (see Sicilia et al. 2012 for more details). The deposited ice mixture thickness is determined by HeNe laser interference measurements following the procedure previously described in Baratta & Palumbo (1998) and Urso et al. (2016). The ice mixture composition ratio is established by calculating the corresponding column densities for each of the individual ice components. With this goal, the individual deposition for each of the ice components is performed, and the corresponding deposition rate is obtained.

2.2 Experimental methods

Gas mixtures are prepared in an all-metal pre-pumped ($<10^{-6}$ mbar) dosing line by serial introduction of the individual gas components into the mixing chamber. Aldrich Chemical 2.0 CO, 2.0 CH_4, 4.0 NH_3, and Air Liquid 5.8 N_2 gas bottles are used as gas-supplies in our experiments. Degased Sigma–Aldrich Chromasolv Plus H_2O and Merck CH_3OH samples are used to obtain H_2O and CH_3OH vapours. Three fill-pump down sequences are performed before introducing the gas mixture into the main chamber. Upon reaching the desired ice thickness, an IR spectrum of the deposited sample is acquired in the range from 7500 to 400 cm^{-1} with 1 cm^{-1} resolution. Two ice thickness values are used in our experiments, ∼0.25 and ∼1.25 μm. Both are well below the penetration depth of 200 keV H^+ and 200 keV He^+ ions according to the SRIM calculation (Ziegler, Biersack & Ziegler 2008). This guarantees a rather uniform energy loss of the ions over the thickness of the ice layer. 200 keV H^+ and He^+ ion beams are generated by a Danfysik 1080-200 ion implanter using Air Liquid H_2 and He gas supplies. The ion beam is electrostatically swept to obtain a uniform irradiation of the sample over an area of about 1 cm^2, significantly larger than the area probed by the IR beam. IR transmittance spectra are acquired after each irradiation step of the ice samples to monitor the destruction of the parent species and formation of the new products. After the ion irradiation a final IR spectrum is acquired and a gradual annealing of the ice at several chosen temperatures is performed. Upon reaching each of the chosen temperatures an IR spectrum is acquired. The experiment is concluded by the acquisition of a final IR spectrum of the refractory organic residue under vacuum at room temperature, the morning after the irradiation.

A selected experiment is repeated using the co-irradiation technique. In this case ices are deposited simultaneously with the ion processing by 60 keV Ar^{2+}. The final ice thickness is significantly higher than the penetration depth of the impinging ions. This results in the formation of an ion processed ice layer significantly thicker than that obtained in regular pre-deposition experiments. Thus, higher amounts of the first generation products are obtained and higher peak-to-noise ratio of the formed product is accessible by IR spectroscopy. See Table 1 with the list of experiments discussed in this study.

2.3 Data analysis

Polynomial baselines are subtracted from all acquired spectra. Subsequently, the band areas corresponding to the selected species present in the ice are calculated. Lorentzian fit is used for deconvolution of HNCO absorption feature (∼2260 cm^{-1}, broad) from the contribution of $^{13}CO_2$ (∼2278 cm^{-1}) and N_2O (∼2242 cm^{-1}) absorption bands. The OCN^- absorption feature (∼2166 cm^{-1}, broad) appears on the obtained IR spectra as the high-wavenumber shoulder of CO absorption band (∼2139 cm^{-1}) and is extracted by subtracting the polynomial fit of CO band from the combined feature. Thus, it should be treated as a conservative estimation of OCN^- absorption. Combined HCN with CN^- (∼2085 cm^{-1}, broad) absorption area is deconvoluted from the contribution of ^{13}CO (∼2092 cm^{-1}) absorption band in the following way. At first, the total area of ^{12}CO band is calculated in each of the recorded spectra. Then the ratio between ^{12}CO and ^{13}CO absorption bands obtained for non-irradiated CO ice is used to derive the contribution of ^{13}CO absorption band to the combined HCN + CN^- + ^{13}CO absorption feature. Consequently, the desired area of the combined HCN + CN^- absorption feature is evaluated. Hereafter, this absorption feature is referred as HCN/CN^-. It should be noted that HCN and CN^- absorption bands cannot be successfully deconvoluted in most of the performed experiments, see Noble et al. (2013).

Column densities of the species are derived from corresponding band areas using the band strength values available from the literature, see Table 2. Calculated column densities are normalized to the initial amount of CH_3OH or CH_4 molecules, and are plotted as a function of irradiation dose given in eV per 16 unified atomic mass units (u). SRIM calculations are used to estimate the stopping power in units of eV cm^2 $molecule^{-1}$ (Ziegler, Biersack & Ziegler 2008). This allows to compare the formation trends of the same species from different experiments and, consequently, to establish the dependence on ice composition.

Table 1. List of performed experiments.

No.	Ice composition	Ratio	Irradiation	Type	Ice thickness
1.1	$CH_3OH:N_2$	1:1	200 keV H^+	'Predeposition'	0.25 μm
1.2	$CH_3OH:N_2$	1:1	60 keV Ar^{2+}	'Codeposition'	–
2	$CO:CH_4:N_2$	1:1:1	200 keV H^+	'Predeposition'	1.2 μm
3	$CO:CH_4:N_2$	1:1:1	200 keV He^+	'Predeposition'	1.2 μm
4	$H_2O:CH_4:N_2$	1:1:1	200 keV H^+	'Predeposition'	1.3 μm
5	$H_2O:CH_4:NH_3$	1:1:1	200 keV H^+	'Predeposition'	1.2 μm

3 RESULTS AND DICUSSION

3.1 Energetic processing of 'CO-rich' ices

Two initial ice molecular compositions are chosen to address the formation of the selected 'CN-bearing' species in 'CO-rich' ice layers. These are $CH_3OH:N_2$ and $CO:CH_4:N_2$ ice mixtures. Fig. 1 presents the results obtained after ion processing of the mixed $CH_3OH:N_2$ ice. All the shown experiments are performed using $CH_3OH:N_2$ ratio of 1:1. In the top panel the fragments of three IR spectra in the range from 2370 to 2000 cm^{-1} are presented. The choice of this spectral range for the quantitative analysis is explained by the presence of the molecule specific stretching vibration modes of (iso)cyanates and cyanides in opposite to the molecule non-specific O–H, N–H, and C–H stretching vibrations appearing at higher wavenumbers. The latter stretching vibration modes are, moreover, strongly affected by H···O and H···N hydrogen bonds that typically result in a widening and a red-shift of the corresponding IR absorption features. Fig. 1(a) shows the IR spectrum of 0.25 μm untreated $CH_3OH:N_2$ ice deposited at 16 K obtained in experiment 1.1. No absorption features can be observed in the presented fragment of the IR spectrum. All of the CH_3OH absorption bands lie outside of the chosen range. These are the strong absorption band at 1039 cm^{-1} (ν_2), the broad absorption feature at 1465 cm^{-1} originating

Table 2. Band strength values used in this study.

Species	Vibration mode (wavenumber)	Band strength (cm mol^{-1})	Reference
CO	(2139 cm^{-1})	1.1×10^{-17}	Jiang et al. (1975)
CO_2	ν_3 (2343 cm^{-1})	7.6×10^{-17}	Yamada & Person (1964)
CH_3OH	ν_2 (1034 cm^{-1})	1.3×10^{-17}	Palumbo, Castorina & Strazzulla (1999)
CH_4	ν_4 (1302 cm^{-1})	6.4×10^{-18}	Mulas et al. (1998)
H_2O	Libration (760 cm^{-1})	3.1×10^{-17}	Gerakines et al. (1995)
NH_3	ν_3 (1070 cm^{-1})	1.8×10^{-17}	Kerkhof, Schutte & Ehrenfreund (1999)
HNCO	ν_3 (2260 cm^{-1})	7.2×10^{-17}	van Broekhuizen, Keane & Schutte (2004)
OCN^-	ν_3 (2170 cm^{-1})	1.3×10^{-16}	van Broekhuizen, Keane & Schutte (2004)
HCN	ν_3 (2085 cm^{-1})	1.1×10^{-17}	Moore & Hudson (2003)
HNC	ν_3 (2035 cm^{-1})	5.1×10^{-18}	Moore & Hudson (2003)

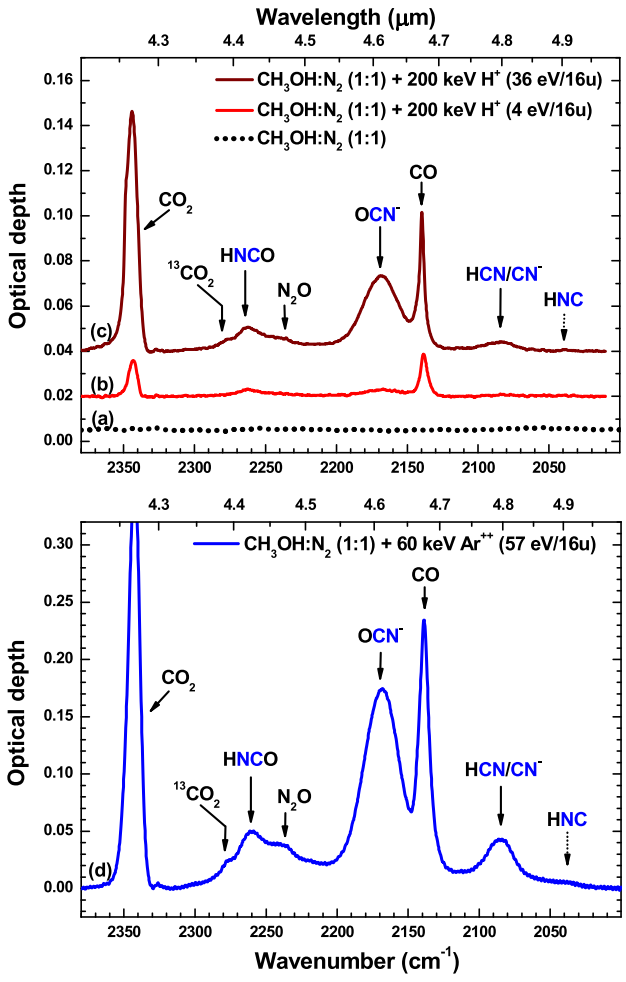

Figure 1. Top panel: fragment of IR spectra obtained in experiment 1.1 after: (a) deposition of $CH_3OH:N_2$ (1:1) ice at 16 K; (b) irradiation of the deposited $CH_3OH:N_2$ (1:1) ice by 200 keV protons with 4 eV/16 u dose; (c) irradiation of the deposited $CH_3OH:N_2$ (1:1) ice by 200 keV protons with a 36 eV/16 u dose. Spectra are plotted with an offset. Bottom panel: (d) fragment of IR spectrum obtained after co-irradiation of deposited $CH_3OH:N_2$ (1:1) ice by 60 keV Ar^{2+} ions with 57 eV/16 u dose (experiment 1.2). The HNC assignment is tentative and indicated by dotted arrow.

from few vibration modes (ν_6, ν_4, ν_5, ν_{10}) and the strong absorption bands in the range of the O–H and C–H stretching vibrations (600–2700 cm^{-1}). Ion processing of the deposited $CH_3OH:N_2$ ice results in the gradual decrease of CH_3OH absorption features and the simultaneous appearance of new absorption bands, originating from newly formed products (see Figs 1b and c). Along with the formation of carbon-bearing species originating solely from CH_3OH, such as CO_2 ($\nu_3 = 2344$ cm^{-1}) and CO (2140 cm^{-1}), few 'CN-bearing' species can be successfully assigned in the shown fragment of the spectra. HNCO and OCN^- can be identified by their strong absorption bands at 2262 cm^{-1} (ν_2) and 2169 cm^{-1} (ν_3), respectively (van Broekhuizen et al. 2005; Islam, Baratta & Palumbo 2014). While the absorption band at 2085 cm^{-1} can be assigned to both HCN (ν_3) and its anion CN^- (Noble et al. 2013), see Section 2.3 for more details. Unfortunately, the aforementioned overlap between the C–H stretching vibration mode of HCN (3100 cm^{-1}) and the C–H stretching modes of CH_3OH presented in irradiated samples does not allow to further constrain HCN assignment. While the reference spectra obtained for the pure HCN ice and for the HCN ice mixtures with H_2O or NH_3 (where hydrogen bonds are also formed) indicates that HCN bending mode (823 cm^{-1}) is too weak to be observed at our experimental conditions, see Gerakines, Moore & Hudson (2004) and Mastrapa, Bernstein & Sandford (2006). Traces of HNC can be tentatively identified at higher irradiation doses by its distinct absorbance feature at 2037 cm^{-1} (ν_3, Milligan & Jacox 1967; Kameneva, Tyurin, & Feldman 2016). Assignment of the latter absorption feature to HNC can be contested by HCNNH assignment, however, preference here is given to the formation of simpler species requiring less intermediate steps to be formed.

To better constrain the assignments of the aforementioned species the additional experiment (experiment 1.2) is performed using co-irradiation technique (see Section 2.2). In this case a much thicker ice is grown, consequently, higher column densities of the products can be obtained to allow their unambiguous identification. However, kinetic analysis of the formation rates in co-irradiation experiments is challenging. The lower panel of Fig. 1 presents the IR spectrum obtained after co-irradiation of $CH_3OH:N_2$ ice with a dose of 57 eV/16 u (Palumbo, Pendleton & Strazzulla 2000). The absorption features previously assigned in Fig. 1(b) and (c) are distinctly visible on the IR spectrum presented in Fig. 1(d) (see Table 3 for the full list of the suggested assignments in Fig. 1). In addition, the N_2O absorption feature at 2242 cm^{-1} can be clearly distinguished.

It should be noted, however, that OCN^- and CN^- counterions cannot be confidently assigned in the obtained IR spectra.

The results obtained after ion irradiation of a $CO:CH_4:N_2$ ice mixture with 200 keV protons (experiment 2) are presented in Fig. 2. This figure shows the fragments of IR spectra in the range from 2370 to 2000 cm^{-1} obtained after the deposition of $CO:CH_4:N_2$ (1:1:1) ice mixture and consequent irradiation of this ice mixture by 200 keV H^+ ions. Similar to Fig. 1, the choice of this spectral range is explained by the presence of the molecule specific

Table 3. List of the IR absorption features presented in Fig. 1 with the corresponding assignments.

Species	$CH_3OH:N_2$	References	Species	$CH_3OH:N_2$	References
CO_2	2342	[I]	HNCO	2262	[IV]
$^{13}CO_2$	2278	[I]	OCN^-	2169	[V]
CO	2138	[II]	HCN	2085	[VI], [VII] [VIII]
N_2O	2242	[III]	CN^-	2085	[VIII], [XI]
			HNC	2037	[VII], [X]

Notes. [a]HCN and CN^- absorbance feature cannot be successfully deconvoluted in these experiments.
[b]Tentative or contested assignments.
[I] – Berney & Eggers 1964, [II] – Jiang et al. 1975, [III] – Dows 1957, [IV] – Teles et al. 1989, [V] – van Broekhuizen et al. 2005, [VI] – Shimanouchi 1972, [VII] – Milligan & Jacox 1967, [VIII] – Moore & Hudson 2003, [XI] – Noble et al. 2013, [X] – Kameneva, Tyurin, & Feldman 2016.

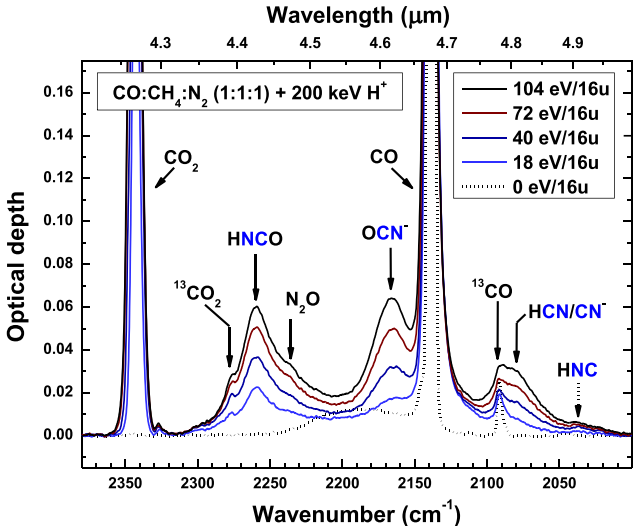

Figure 2. *Dotted line* – fragment of IR spectrum obtained in experiment 2 after deposition of $CO:CH_4:N_2$ (1:1:1) ice at 17 K; *solid lines* – fragment of IR spectra obtained after irradiation of the deposited $CO:CH_4:N_2$ (1:1:1) ice by 200 keV protons with several indicated irradiation doses. The HNC assignment is tentative and indicated by dotted arrow.

stretching vibration modes of (iso)cyanates and cyanides. All the products previously identified after irradiation of $CH_3OH:N_2$ (1:1) mixed ice (Fig. 1) can also be successfully assigned on the IR spectra obtained after ion irradiation of $CO:CH_4:N_2$ (1:1:1) ice (Fig. 2). Among the 'CN-bearing' species only CH_3CN (2262, 1437, 1046, 918 cm^{-1}, Shimanouchi 1972), CH_3NC (2169, 1465, 1124 cm^{-1}, Shimanouchi 1972), and CH_3NCO (2163 cm^{-1}, Pasinszki & Westwood 1995) may potentially contribute to the absorption features presented in Fig. 2. However, formation of either CH_3CN, CH_3NC or CH_3NCO requires participation of all three ice constituents CH_4, CO, and N_2. Therefore, the preference is given to the assignments of simpler products and products with less carbon atoms. Thus, only HNCO, OCN^-, and HCN/CN^- can be unambiguously assigned in Fig. 2. This list can be concluded with the tentative assignment of HNC that for the same reasons should be preferable over the assignment of more complex HCNNH molecule. In addition, the strongest absorption feature of N_2O oxide (2239 cm^{-1}) can be distinguished on the IR spectra presented in Fig. 2. Repetition of the $CO:CH_4:N_2$ ice irradiation experiment using 200 keV He^+ ions (experiment 3) does not result in any qualitative changes in the experimental results.

3.2 Energetic processing of 'H_2O-rich' ices

Experiments 4 and 5 are performed to investigate formation of 'CN-bearing' species upon ion irradiation of 'H_2O-rich' ices and the results of these experiments are summarized in Fig. 3. In this figure the fragments of IR spectra obtained after the deposition of $H_2O:CH_4:N_2$ and $H_2O:CH_4:NH_3$ ice mixtures of 1:1:1 ratio, along with the fragments of IR spectra obtained after irradiation of these ices by 200 keV H^+ ions are presented, see left-hand and right-hand panels of Fig. 3, respectively. Substitution of CO molecules in $CO:CH_4:N_2$ ice mixtures, see Fig. 2, with H_2O molecules, see left-hand panel of Fig. 3, does not change the results of the corresponding ion irradiation experiments from the qualitative point of view. Similar species can be identified among the products of irradiation. The list of detected 'CN-bearing' species are comprised by HNCO, OCN^-, HCN/CN^- and traces of HNC, see Table 4 for more details. The following differences with $CO:CH_4:N_2$ ice irradiation experiments can be stressed (see experiment 2). In opposite to the $CO:CH_4:N_2$ ices irradiation experiments significant overabundance of OCN^- over HNCO is observed, that is not surprising taking into account that H_2O molecules can act as a weak base accepting the proton from HNCO acid to yield OCN^- (Novozamsky, Schutte & Keane 2001; van Broekhuizen et al. 2005; Theule et al. 2011).

The use of NH_3 instead of N_2 as a source of nitrogen (see right-hand panel of Fig. 3) results in a further decrease of the HNCO absorption feature and the corresponding growth of OCN^-/HNCO ratio. Here, a lower relative HNCO formation yield than in both $CO:CH_4:N_2$ and $CH_3OH:N_2$ ice irradiation experiments is observed. This is consistent with the increase of NH_3 base strength in comparison to H_2O. Moreover, the presence of NH_3 base as one of the initial component in the ice may also explain the lack of HNC traces. HNC can be efficiently converted into CN^- upon formation following acid–base reaction with NH_3 (Noble et al. 2013). These acid–base reactions will be further addressed in Section 3.3. Due to the overlaps of NH_4^+ and H_3O^+ absorption features with the absorption features of other species present in the ice, neither of these counterions can be unambiguously assigned in our experiments. Absence of N_2 as the initial component in the irradiated ice mixture also results in the lack of N_2O detection, see left-hand panel of Fig. 3 for comparison.

3.3 Obtained kinetic curves and discussion

Calculated HNCO and OCN^- column densities (see Section 2.3 for more details) are normalized to the initial amount of CH_3OH or CH_4 molecules and plotted versus irradiation dose given in eV per 16 u, see upper panel of Fig. 4. Given the direct chemical link between HNCO and OCN^-:

$$\mathrm{HNCO} + \mathrm{M} \rightarrow \mathrm{OCN^-} + \mathrm{HM^+}\ (\text{where M is a base, e.g. } \mathrm{NH_3}, \mathrm{H_2O}, \text{etc.}), \quad (1)$$

a combined normalized abundance of both species is also plotted on the upper-right panel to highlight the evolution of the total yield of both species with applied irradiation dose. Lower panels of Fig. 4 present the evolution of the HNCO, OCN^-, and their combined column densities with the gradual annealing of the ice after completion of the ion irradiation experiments. In this case, normalization to the initial amounts of the species prior to the thermal processing is performed under the assumption that the used band strength values are independent of the temperature.

Few experimental observations can be revealed from the analysis of the kinetic curves. In the 'CO-rich' ices HNCO is either

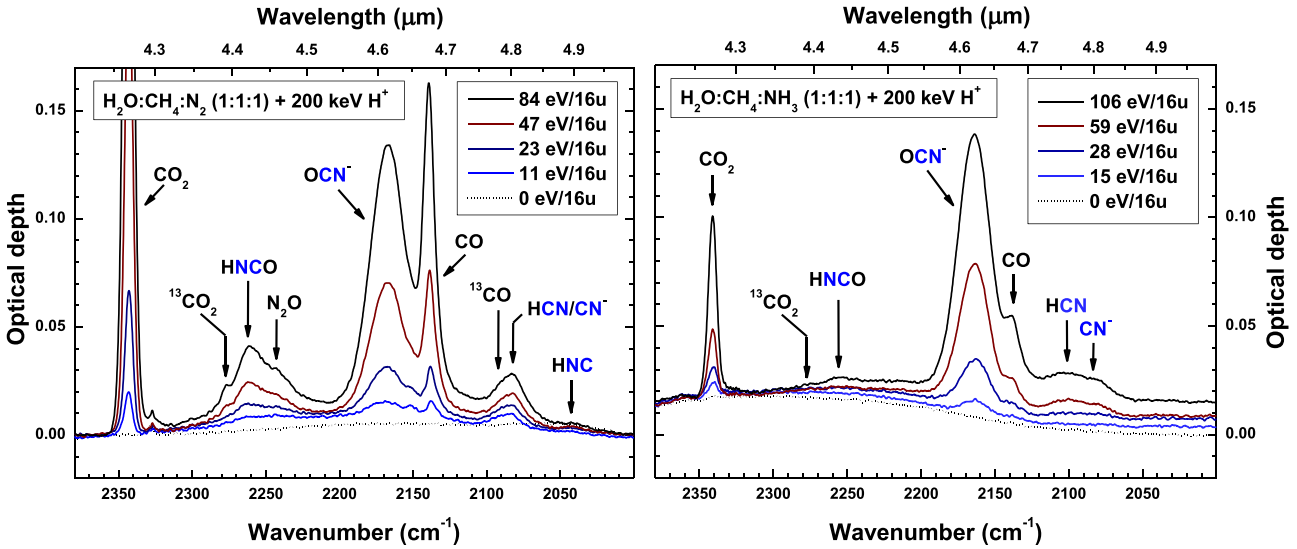

Figure 3. Left-hand panel. *Dotted line* – fragment of IR spectra obtained in experiment 4 after deposition of H_2O:CH_4:N_2 (1:1:1) ice at 17 K; *solid lines* – fragment of IR spectra obtained after irradiation of the deposited H_2O:CH_4:N_2 (1:1:1) ice by 200 keV protons with several indicated irradiation doses. The HNC assignment is tentative and indicated by dotted arrow. Right-hand panel. *Dotted line* – fragment of IR spectra obtained in experiment 5 after the deposition of H_2O:CH_4:NH_3 (1:1:1) ice at 17 K; *solid lines* – fragment of IR spectra obtained after irradiation of the deposited H_2O:CH_4:NH_3 (1:1:1) ice by 200 keV protons with several indicated irradiation doses.

Table 4. List of the IR absorption features assigned to CN-bearing species and N_2O in the performed ice irradiation experiments.

Species	CH_3OH:N_2	CO:CH_4:N_2	H_2O:CH_4:N_2	H_2O:CH_4:NH_3	References
HNCO	2262	2259	2261	2257	[I], [II]
OCN^-	2169	2166	2167	2164	[III]
HCN	2085[a]	2084[a]	2082[a]	2101	[II], [IV], [V]
CN^-	2085[a]	2084[a]	2082[a]	2085	[V], [VI]
HNC	2037	2037	2043	n.d.	[IV], [VII]
N_2O	2242	2239	2242	n.d.	[VIII]

[a]HCN and CN^- absorption feature cannot be successfully deconvoluted in these experiments.
n.d. – not detected.
[I] – Teles et al. 1989, [II] – Shimanouchi 1972, [III] – van Broekhuizen et al. 2005, [IV] – Milligan & Jacox 1967, [V] – Moore & Hudson 2003, [VI] – Noble et al. 2013, [VII] – Kameneva, Tyurin, & Feldman 2016, [VIII] – Dows 1957.

equally or preferably formed over OCN^-. The shape of the HNCO kinetic curves in 'CO-rich' ice mixtures indicates direct formation of HNCO from the initial ice components, while the OCN^- formation trends reveal that generally OCN^- start to build up at higher doses from the first generation products. This is consistent with the formation of OCN^- from HNCO following reaction (1), where M is the base present in the ice during irradiation (van Broekhuizen et al. 2005; Bennett et al. 2010; Theule et al. 2011). Analysis of HNCO and OCN^- formation trends in 'H_2O-rich' ices shows that both species are formed at higher dose and require the precursor species to be produced first in the ice. Thus, their formation should be inefficient at low irradiation doses.

Thermal processing of the ice upon irradiation shows that for all the performed experiments steady decrease of HNCO and corresponding increase of OCN^- abundance is observed while the combined column density stays almost unaffected. This observation is fully in line with the conversion of formed HNCO into OCN^- according to reaction (1). This reaction, on one hand, is induced by thermal processing itself and, on the other hand, is promoted by the desorption of high-volatile components that isolate HNCO acid from the bases available for the reaction.

Strong pieces of evidence in favour of reaction (1) further constrain HNCO and OCN^- assignments through Figs 1–3. Assignments of OCN stretching vibration mode of R-OCN (R = CH_3, C_2H_5, etc.) and CN stretching vibration mode of R-CN (R = CH_3, C_2H_5, etc.) to the whole absorbance feature around 2260 cm^{-1} is improbable. R-OCN or R-CN solely cannot explain conversion into OCN^- upon thermal processing, and require HNCO to be present in the ice. Furthermore, a lower limit on the HNCO content can be derived from the decrease of the normalized HNCO column density upon thermal processing (see lower left panel of Fig. 4). For example, a complete drop of HNCO abundance in CH_3OH:N_2 (1:1) ice irradiation experiments with gradual heat up of the ice to 150 K indicates that the whole 2260 cm^{-1} feature can be unambiguously assigned to HNCO in this experiment. *Vice versa*, an upper limit on R-OCN or R-CN yields can be drawn from the data presented on the lower panel of Fig. 4 by evaluating the fraction of unconverted 'HNCO'. The same is true for the possible presence of

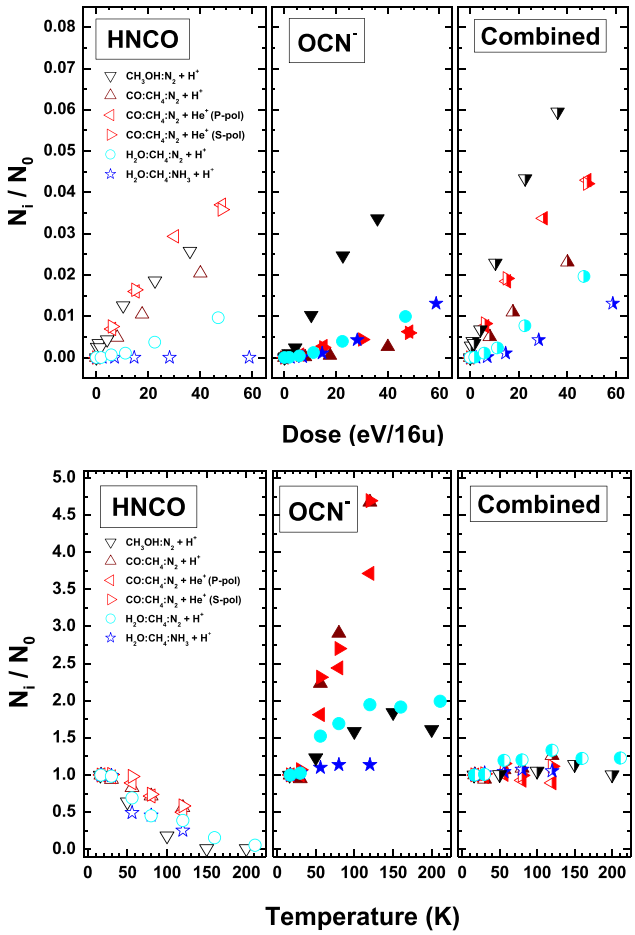

Figure 4. Top panel: normalized abundance of HNCO (left), OCN^- (central), and the sum of both species (right), produced after: *black down triangles* – irradiation of $CH_3OH:N_2$ (1:1) ice mixture with 200 keV H^+ (experiment 1.1); *wine up triangle* – irradiation of $CO:CH_4:N_2$ (1:1:1) ice mixture with 200 keV H^+ (experiment 2); *red left triangles* – irradiation of $CO:CH_4:N_2$ (1:1:1) ice mixture with 200 keV He^+ (P-polarized IR beam, experiment 3); *red right triangles* – irradiation of $CO:CH_4:N_2$ (1:1:1) ice mixture with 200 keV He^+ (S-polarized IR beam, experiment 3); *cyan circles* – irradiation of $H_2O:CH_4:N_2$ (1:1:1) ice mixture with 200 keV H^+ (experiment 4); *blue stars* – irradiation of $H_2O:CH_4:NH_3$ (1:1:1) ice mixture with 200 keV H^+ (experiment 5). Irradiation of ice mixtures is carried out at 17 K, with $CH_3OH:N_2$ ice irradiation done at 16 K. Normalization is performed to the initial CH_4 or CH_3OH abundance. Bottom panel: evolution of abundance of HNCO (left), OCN^- (central), and the sum of both species normalized after addition (right) with annealing of the ice. The values are normalized to the final abundance of the species obtained in the experiments showed on the top panel and keep the same labelling.

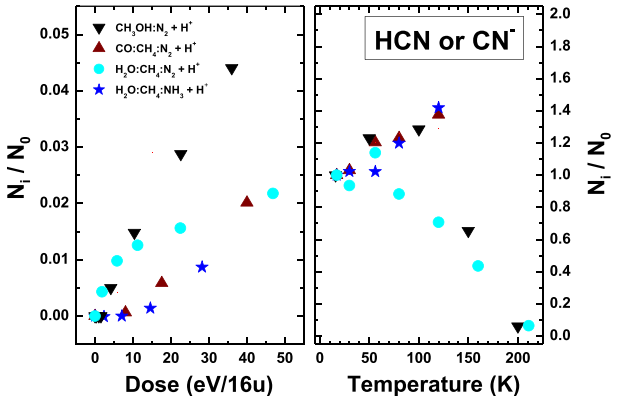

Figure 5. Left-hand panel: normalized HCN/CN^- abundance produced after: *black down triangles* – irradiation of $CH_3OH:N_2$ (1:1) ice mixture with 200 keV H^+ (experiment 1.1); *wine up triangles* – irradiation of $CO:CH_4:N_2$ (1:1:1) ice mixture with 200 keV H^+ (experiment 2); *cyan circles* – irradiation of $H_2O:CH_4:N_2$ (1:1:1) ice mixture with 200 keV H^+ (experiment 4); *blue stars* – irradiation of $H_2O:CH_4:NH_3$ (1:1:1) ice mixture with 200 keV H^+ (experiment 5). Irradiation of ice mixtures is carried out at 17 K, with $CH_3OH:N_2$ ice irradiation done at 16 K. Normalization is performed to the initial CH_4 or CH_3OH abundance. Right-hand panel: evolution of HCN/CN^- abundance with annealing of the ice. The values are normalized to the final abundance of the species obtained in the experiments showed on the left-hand panel and keep the same labelling.

R-NC (R = CH_3, C_2H_5, etc.) in the ice at the end of irradiation. The assignment of CN stretching vibration mode of R-CN to the absorption feature centered around 2160 cm^{-1} is contested with OCN^-. The upper limits on R-NC abundance can be evaluated assuming that prior to the gradual warm up of the ice the IR feature around 2160 cm^{-1} is solely explained by R-NC contribution, and OCN^- build up occurs as the result of the thermal processing. It should be stressed, however, that these upper limits would correspond to the ice composition at the end of irradiation experiment, but not for the intermediate points and, thus, their analysis lies outside of the scope of this work. Here, the preference is given to the assignments of simpler species, i.e. HNCO and OCN^-. These assignments are also justified by the fact that low irradiation doses (<10 eV/16 u) are investigated in this study. Low irradiation doses are not in favour of heavy organic molecule formation requiring interaction between several parent species. Under our experimental conditions, the normalized abundance of OCN^- at the end of irradiation experiment depends on the initial mixture and lies in the range from 0.003 to 0.03 (see Fig. 4, top central panel). Bennett et al. (2010) performed irradiation of NH_3:CO ice using energetic electrons (5 keV) and reported formation of OCN^- with a comparable normalized abundance of 0.02 at the end of irradiation.

Similarly to the calculation of HNCO and OCN^- column densities, the broad absorption feature around 2080 cm^{-1} is used to evaluate combined HCN and CN^- abundance. In opposite to the case of HNCO and OCN^-, absorption bands of HCN and CN^- cannot be easily deconvoluted (Noble et al. 2013). Therefore, only the combined abundance of both species can be estimated. Furthermore, CN^- has ∼1.6 stronger absorption band strength over that of HCN molecule (Moore & Hudson 2003; Noble et al. 2013). This means that if the conversion of HCN into CN^- occurs upon thermal or ion processing of the ice following reaction:

$$HCN + M \rightarrow CN^- + HM^+ \text{ (where M is a base)}, \quad (2)$$

the rise in the area of the combined IR absorption feature will be observed despite unchanged combined column density of both species. This should be taken into account while analysing formation trends presented in Fig. 5. Only HCN absorbance band strength value is used to calculate the normalized column densities for simplicity, see Section 2.3 for more details. The rise of the normalized abundance with gradual heating until 120 K indicates that conversion of HCN into CN^- following reaction (2) occurs, while the drop in the abundance at higher temperatures is explained by the desorption of both species. As for the dependence of the column density on the applied irradiation dose, only the observation on the

Table 5. Normalized formation yields[a] obtained as the result of experimental data interpolation.

	$CH_3OH:N_2$ (1:1)			$CO:CH_4:N_2$ (1:1:1)			$H_2O:CH_4:N_2$ (1:1:1)			$H_2O:CH_4:NH_3$ (1:1:1)		
Dose (eV/16 u)	0.05	0.5	5	0.05	0.5	5	0.05	0.5	5	0.05	0.5	5
HNCO	5×10^{-5}	5×10^{-4}	5×10^{-3}	3×10^{-5}	3×10^{-4}	3×10^{-3}	5×10^{-6}	5×10^{-5}	5×10^{-4}	–	–	–
OCN^-	3×10^{-5}	3×10^{-4}	3×10^{-3}	2×10^{-6}	2×10^{-5}	2×10^{-4}	4×10^{-6}	4×10^{-5}	4×10^{-4}	2×10^{-6}	2×10^{-5}	2×10^{-4}
HCN/CN^-	7×10^{-5}	7×10^{-4}	7×10^{-3}	1×10^{-5}	1×10^{-4}	1×10^{-3}	1×10^{-4}	1×10^{-3}	1×10^{-2}	3×10^{-6}	3×10^{-5}	3×10^{-4}

[a]Formation yield is the column density of a given species divided by the initial column density of one of the parent species.

relative formation efficiency between the irradiation experiments can be concluded. A clear discrimination between conversion of the formed HCN into CN^- over the course of irradiation or involvement of the additional formation routes from first generation products is challenging. However, the following conclusions still can be drawn. The kinetic curves presented in Fig. 5 indicate that energetic processing of $CH_3OH:N_2$ (1:1) and $H_2O:CH_4:N_2$ (1:1:1) ice mixtures is significantly more effective in the formation of cyanic acid or its anion than two other experimentally tested ice compositions. In the two later cases, i.e. irradiation of $CO:CH_4:N_2$ (experiment 4) and $H_2O:CH_4:NH_3$ (experiment 5) ice mixtures, efficient formation of HCN and CN^- occur at high irradiation doses. This hints on the formation of both of the species from the precursors obtained at the earlier stage of irradiation.

4 ASTROCHEMICAL IMPLICATIONS AND CONCLUSIONS

The performed laboratory-based research aims at better understanding of cosmic ray induced solid-state N_2 chemistry in cold dark clouds and prestellar cores. The main goal perceived by this study is the acquisition of formation yields for the few chosen 'CN-bearing' species for the relevant irradiation doses. The obtained values are intended to be used for the future JWST data interpretation, and to provide the indirect probe of N_2-presence in the interstellar ices. With this goal, few selected ice mixtures are irradiated with 200 keV H^+ and He^+ ions to mimic cosmic ray processing of the icy grain mantles. The choice of ice mixtures irradiated in our experiments is aimed to address the composition of the ice layers formed in two distinct ice formation stages in cold dark clouds (Boogert, Gerakines & Whittet 2015). These are 'H_2O-rich' and 'CO-rich' ices discussed in section 3.

In present study we focus on the quantitative analysis of four formed 'CN-bearing' species detected in the performed experiments. These are HNCO, OCN^-, and HCN/CN^-. The latter two species cannot be spectroscopically deconvoluted in this study (Noble et al. 2013), thus, the combined abundance of both species is evaluated. The traces of the fifth one, HNC, can only be tentatively assigned in the experiments involving solid N_2, while lack completely in the experiment involving solid NH_3. This prohibits quantitative analysis of this species. Formation of another 'CN-bearing' species, H_2NCHO, is not discussed here in view of the recent report by Kaňuchová et al. (2016) and Urso et al. (2017).

The doses relevant to the prestellar stages of star formation depend on the accepted ionization rate and are typically below 1 eV/16 u for the time frames of the collapse of dense core (Moore 1999). A near linear grow of HNCO, OCN^-, and HCN/CN^- yields is observed at low irradiation doses. Therefore, a simple linear fit through the beginning of the kinetic curves followed by an interpolation is used to obtain the corresponding formation yields for each of the species at low irradiation doses. Table 5 presents the results of interpolation for each of the studied initial ice composition. Derived formation yields are presented for the total irradiation doses equal to 0.05, 0.5, and 5 eV/16 u. Assuming the cosmic ray flux of 1 MeV proton cm^{-2} s^{-1} and the ice mantle thickness of 20 nm, the aforementioned irradiation doses would be accumulated over $\sim 2 \times 10^5$, $\sim 2 \times 10^6$, and $\sim 2 \times 10^7$ yr, respectively (Moore 1999; Kaňuchová et al. 2016).

It should be stressed that in order to derive the initial yields an interpolation of the initial part of the kinetic curves is required. In contrast, a simple scale down of the final abundances (obtained at high irradiation dose) to these low irradiation doses results in a significant deviations from the results of interpolation. The latter is explained by the ongoing evolution of the ice composition upon further irradiation. That results in the appearances of both new formation and destruction pathways for the discussed species.

Combined formation yields of HNCO and OCN^- in CO- and CH_3OH-rich ices are found to be significantly higher than corresponding yields in 'H_2O-rich' ices. Moreover, ion irradiation of $CH_3OH:N_2$ ice results in the highest yields of both HNCO and OCN^- that are one order of magnitude higher than that in the mixtures containing H_2O. This is consistent with the current observational data towards low- and high-mass YSOs showing that OCN^- is present in the 'CO-rich' layer of the ice mantle, rather than being mixed with H_2O ice, see Öberg et al (2011) and Boogert, Gerakines & Whittet (2015). The direct comparison between the chemical yields presented in Table 5 and the OCN^- abundance in low- and high-mass YSOs, however, is not trivial. The ice mantles in YSOs undergoes significant thermal processing. The latter should result in the substantial conversion of the formed HNCO into OCN^-, in accordance with the reaction (1). Therefore, the combined HNCO with OCN^- yield should be compared with the OCN^- observations towards YSOs. With the applied ionization rate of 3×10^{-17} ionizations s^{-1} (Moore 1999; Kaňuchová et al. 2016) a period of ~ 1–10×10^7 yr is required to reach the relative abundance of OCN^- reported by Boogert, Gerakines & Whittet (2015) for low- and high-mass YSOs. With the ionization rate of 1.3×10^{-15} ionizations s^{-1} the period is deduced to be 2.5–25 $\times 10^5$ yr. That is comparable to the time frames of the dense core collapse. Alternatively, a significant period of cosmic-ray processing prior to the core collapse assuming low ionization rate is required to meet these abundances by N_2-induced chemistry, unless other HNCO or OCN-formation routes (van Broekhuizen et al. 2005; Fedoseev et al. 2016) are at play simultaneously.

A detailed look on the data presented in Table 5 shows that the formation yields of HNCO in the ice mixtures containing CO and CH_3OH ices are higher than OCN^- formation rates (in $\sim$15 and $\sim$2 times, respectively). In 'CO-rich' interstellar ice analogues most of the formed isocyanate is locked in the form of HNCO and will require thermal processing before conversion into OCN^-. On the contrary, in 'H_2O-rich' ices the formation rate of OCN^- is significantly higher than that of HNCO. Moreover, in the presence of NH_3 near all isocyanate is locked in OCN^-. So far there is no

successful search for HNCO or OCN^- towards background stars. This is caused by the limited sensitivity of the technique allowing only the upper limit on OCN^- abundance (<0.5 with respect H_2O) to be provided (Boogert, Gerakines & Whittet 2015). If future background star observations using JWST will result in the detection of HNCO and OCN^- in cold dark clouds or prestellar cores, the individual values for HNCO and OCN^- formation yields should be applied. This stands as long as no thermal processing is experienced by the ice mantle.

Efficient formation of OCN^- and CN^- in some of the performed experiments is likely explained by the significant excess energy of the species produced after impinging of the ion, allowing conversion of the formed HNCO and HCN/HNC acids into OCN^- and CN^- anions following reactions (1) and (2). Similar proton transfer upon irradiation of NH_3:CO and CH_3NH_2:CO_2 ices by energetic 5 keV electrons is discussed, for example, in Bennett et al. (2010). On the other hand, this excess energy can simultaneously be responsible for the partial desorption of the ice material (including newly formed species) into the gas phase (Bringa & Johnson 2000; Ivlev et al. 2015; Muntean et al. 2016). Thus, providing a mechanism how gas-phase can be enriched by newly formed CN-bearing species. This, however, is the subject for dedicated research work using techniques suitable for the gas phase analysis of the released material.

In view of the upcoming JWST observations towards cold dark clouds the obtained findings can be summarized in the following points:

(i) The obtained HNCO/OCN^- ratios (see Table 5) can be used as the tracers of N_2 presence.

(ii) Co-formation of N_2O in N_2-containg ices serves as the discriminator between N_2 and NH_3 precursors for OCN^- formation.

(iii) Unless formation of OCN^- occurs in 'H_2O'-rich ice layer of icy grain mantle, HNCO should always be observed simultaneously with OCN^-.

ACKNOWLEDGEMENTS

This research was supported through the Progetto Premiale 2012 'iALMA' grant (CUP C52I13000140001) approved by Ministero dell'Istruzione, dell'Università e della Ricerca, through the financial support from the European Union's Horizon 2020 research and innovation programme under the Marie Skłodowska-Curie actions grant agreement n. 664931, through the funding from the European Community's Seventh Framework Programme (FP7/2007–2013) under grant agreement no. 238258 (LASSIE), and by the Italian Space Agency (ASI) contract no. 2013–073-R.0: PSS (Photochemistry on the Space Station).

REFERENCES

Baratta G. A., Palumbo M. E., 1998, J. Opt. Soc. Am. A, 15, 3076
Baratta G. A., Chaput D., Cottin H., Fernandez Cascales L., Palumbo M. E., Strazzulla G., 2015, Planet. Space Sci., 118, 211
Belloche A., Menten K. M., Comito C., Müller H. S. P., Schilke P., Ott J., Thorwirth S., Hieret C., 2008, A&A, 482, 179
Bennett C. J., Jones B., Knox E., Perry J., Kim Y. S., Kaiser R. I., 2010, ApJ, 723, 641
Berney C. V., Eggers D. F., Jr, 1964, J. Chem. Phys. 40, 990
Boogert A. C. A, Blake G. A., Tielens A. G. G. M., 2002. ApJ, 577, 271
Boogert A. C. A., Gerakines P. A., Whittet D. C. B., 2015, ARA&A, 53, 541
Bringa E. M., Johnson R. E., 2000, Surf. Sci., 451, 108
Chang Q., Herbst E., 2012, ApJ, 759, 147
Danger G., Borget F., Chomat M., Duvernay F., Theulé P., Guillemin J.-C., Le Sergeant D'Hendecourt L., Chiavassa T., 2011, A&A, 535, A47
Demyk K., Dartois E., D'Hendecourt L., Jourdain de Muizon M., Heras A. M., Breitfellner M., 1998, A&A, 339, 553
Dows D. A., 1957, J. Chem. Phys., 26, 745
Elsila J., Allamandola L. J., Sandford S. A., 1997, ApJ, 479, 818
Fedoseev G., Ioppolo S., Zhao D., Lamberts T., Linnartz H., 2015, MNRAS, 446, 439
Fedoseev G., Chuang K.-J., van Dishoeck E. F., Ioppolo S., Linnartz H., 2016, MNRAS, 460, 4297
Gerakines P. A., Schutte W. A., Greenberg J. M., van Dishoeck E. F., 1995, A&A, 296, 810
Gerakines P. A., Moore M. H., Hudson R. L., 2004, Icarus, 170, 202
Gibb E. L., Whittet D. C. B., Boogert A. C. A., Tielens A. G. G. M., 2004, ApJS, 151, 35
Ioppolo S., Fedoseev G., Lamberts T., Romanzin C., Linnartz H., 2013, Rev. Sci. Instrum. 84, 073112
Islam F., Baratta G. A., Palumbo M. E., 2014, A&A, 561, A73
Ivlev A. V., Röcker T. B., Vasyunin A., Caselli P., 2015, ApJ, 805, 59
Jiang G. J., Person W. B., Brown K. G., 1975, J. Chem. Phys., 62, 1201
Kameneva S. V., Tyurin D. A., Feldman V. I., 2016, Radiat. Phys. Chem., 124, 30
Kaňuchová Z., Urso R. G., Baratta G. A., Brucato J. R., Palumbo M. E., Strazzulla G., 2016, A&A, 585, A155
Kerkhof O., Schutte W. A., Ehrenfreund P., 1999, A&A, 346, 990
Li X., Heays A. N., Visser R., Ubachs W., Lewis B. R., Gibson S. T., van Dishoeck E. F., 2013, A&A, 555, A14
Mastrapa R. M., Bernstein M. P., Sandford S. A., 2006, Lunar Planet. Sci. Conf., 37, 1378
Matthews C. N., Minard R. D., 2008, in Kwok S., Stanford S., eds, Proc. IAU Symp. 251, Organic Matter in Space. Cambridge Univ. Press, Cambridge, UK, p. 453, and references therein
Mathews G. S. et al., 2013, A&A, 557, A132
Milligan D. E., Jacox M.E., 1967, J. Chem. Phys., 47, 278
Minard R., Yang W., Varma P., Nelson J., Matthews C., 1975, Science, 190, 387
Moore M. H., 1999, in d'Hendecourt L., Joblin C., Jones A., eds, The Physics and Chemistry of Ices in the Interstellar Medium, in Solid Interstellar Matter: The ISO Revolution, Les Houches 11. EDP Sciences, Les Ulis, France, p. 199
Moore M. H., Hudson R. L., 2003, Icarus, 161, 486
Mulas G., Baratta G. A., Palumbo M. E., Strazzulla G., 1998, A&A, 333, 1025
Muntean E. A., Lacerda P., Field T. A., Fitzsimmons A., Fraser W. C., Hunniford A. C., McCullough R. W., 2016, MNRAS, 462, 3361
Noble J. A., Theule P., Borget F., Danger G., Chomat M., Duvernay F., Mispelaer F., Chiavassa T., 2013, MNRAS, 428, 3262
Novozamsky J. H., Schutte W. A., Keane J. V., 2001, A&A, 379, 588
Öberg K. I., Boogert A. C. A., Pontoppidan K. M., van den Broek S., van Dishoeck E. F., Bottinelli S., Blake G. A., Evans N. J., II, 2011, ApJ, 740, 109
Palumbo M. E., Castorina A. C., Strazzulla G., 1999, A&A, 342, 551
Palumbo M. E., Pendleton Y. J., Strazzulla G., 2000, ApJ, 542, 890
Pasinszki T., Westwood N. P. C., 1995, J. Phys. Chem., 99, 1649
Saladino R., Crestini C., Ciciriello F.,, Costanzo, G., di Mauro, E., 2006, Orig. Life Evol. Biosph., 36, 523
Saladino R., Carota E., Botta G., Kapralov, M., Timoshenko, G. N., Rozanov, A., Krasavin, E., Di Mauro, E., 2016, Orig. Life Evol. Biosph., 46, 515
Sandford S. A., Bernstein M. P., Allamandola L. J., Goorvitch D., Teixeira T. C. V. S., 2001, ApJ, 548, 836
Shimanouchi T., Tables of Molecular Vibrational Frequencies Consolidated, Vol. I, National Bureau of Standards, 1972, p. 1.
Sicilia D., Ioppolo S., Vindigni T., Baratta G. A., Palumbo M. E., 2012, A&A, 543, A155
Strazzulla G., Baratta G. A., Palumbo M. E., 2001, Spectrochim. Acta A, 57, 825

Teles J. H., Maier G., Andes Hess B., Schaad L. J., Winnewisser M., Winnewisser B. P., 1989, Chem. Ber., 122, 753
Theule P., Duvernay F., Ilmane A., Hasegawa T., Morata O., Coussan S., Danger G., Chiavassa T., 2011, A&A, 530, A96
Tielens A. G. G. M., Tokunaga A. T., Geballe T. R., Baas F., 1991, ApJ, 381, 181
Urso R. G., Scirè C., Baratta G. A., Compagnini G., Palumbo M. E., 2016, A&A, 594, A80
Urso R. G., Scirè C., Baratta G. A., Brucato J. R., Compagnini G., Kaňuchová Z., Palumbo M. E., Strazzulla G., 2017, Phys. Chem. Chem. Phys., 19, 21759
van Broekhiuzen F. A., Keane J. V., Schutte W. A., 2004, A&A, 415, 425
van Broekhuizen F. A., Pontoppidan K. M., Fraser H. J., van Dishoeck E. F., 2005, A&A 441, 249
Wu Y.-J., Wu R. C., Chou S.-L., Lin M.-Y., Lu H.-C., Lo J.-I., Cheng B.-M., 2012, ApJ, 746, 175
Yamada H., Person W. B., 1964, J. Chem. Phys., 41, 2478
Ziegler J. F., Biersack J. P., Ziegler M. D., 2008, The Stopping and Range of Ions in Solids (New York: Pergamon Press), 321

This paper has been typeset from a Microsoft Word file prepared by the author.